scientific reports

Check for updates

OPEN

Potentiation of immune checkpoint blockade with an ITPP radiosensitizer studied with oxygen saturation measurements from photoacoustic imaging

Renee L. Tran[1,2], Xiaofei Liang[1], Jorge de la Cerda[1], F. William Schuler[1] & Mark D. Pagel[1,3]✉

Hypoxia in the tumor microenvironment hinders antitumor immunity. Increasing tumor oxygenation may promote T cell infiltration and tumor control by immune checkpoint blockade (ICB). We found that a radiosensitizer, myo-inositol trispyrophosphate (ITPP), caused oxygen unloading from hemoglobin in CT26 and 4T1 tumors as indicated by photoacoustic imaging (PAI). This change in hypoxia detected by PAI was correlated with strong positive correlations with CD8+ and CD4+ FoxP3- effector T cell (Teff), and negative correlations with monocyte frequencies, indicating that ITPP promoted more immunogenic tumor microenvironments in both models. Combination ITPP and ICB improved tumor control and survival in both models. Therefore, imaging ITPP-modulated tumor hypoxia with PAI was related to ICB treatment response in these studies. Future combination immunotherapy regimens may benefit from monitoring hypoxia using molecular imaging with PAI.

Keywords Tumor hypoxia, ITPP, Immune checkpoint blockade, Photoacoustic imaging

Immune checkpoint blockade (ICB) treatments have joined surgery, chemotherapy, and radiation therapy as the fourth pillar of cancer treatment[1]. ICB was first approved for patients with advanced melanoma, and ICB is now approved for the treatment of patients with lung lung, prostate, ovarian, cervical, endometrial, and urothelial cancers, as well as hepatocellular and renal cell carcinomas[2–10]. However, ICB is still far from being a reliable cure for cancer. For example, the ICB treatments nivolumab and ipilimumab (the therapeutic antibodies anti-programmed death-1, or αPD-1, and anti-cytotoxic T lymphocyte antigen-4, or αCTLA-4, respectively) induce objective response rates of 58% in melanoma[11], 35.9% in non-small cell lung cancer[12], 42% in renal cell carcinoma[13], 16% in hepatocellular carcinoma[14], and 18% in breast cancer[15]. To increase the efficacy of ICB, more studies are needed to sensitize tumors and identify patients who would be the most responsive to ICB.

Hypoxia in the tumor microenvironment (TME) can contribute to resistance to ICB[16]. Tumor hypoxia recruits and promotes the immunosuppressive function of myeloid-derived suppressor cells (MDSCs)[17,18]. In addition, hypoxia increases the stability and transcriptional activity of hypoxia-inducible factor HIF-1α[19], which subsequently upregulates programmed death ligand-1 (PD-L1) that increases the inhibitory landscape in hypoxic TMEs[20,21]. MDSCs and the increased PD-L1 expression recruited and induced by hypoxia promote the development of immunogenically "cold" tumors by inhibiting T cell function. Hypoxia also causes tumors to become "cold" by directly preventing T cell trafficking into hypoxic regions, inhibiting T cell expansion, inhibiting tumor cell cytotoxicity, and promoting T cell death[22–24]. Efforts have focused on converting "cold" tumors into "hot" tumors that have high T cell penetrance and activity and causing such tumors to respond better to ICB[1,25]. Studies targeting hypoxic regions using hypoxia-activated prodrugs[22], inhibitors of oxidative phosphorylation[26,27], agents for direct oxygenation[28], and oxygen carriers[29], all showed that doing so promotes T cell infiltration and enhances ICB response. However, the extent of hypoxia abrogation necessary to increase ICB efficacy is unclear.

[1]Department of Cancer Systems Imaging, MD Anderson Cancer Center, 1515 Holcombe Blvd., Houston, TX 77030, USA. [2]University of Texas Graduate School of Biomedical Sciences, Houston, TX, USA. [3]Department of Medical Physics, University of Wisconsin, Madison, WI 53705, USA. ✉email: mdpagel2@wisc.edu

Myo-inositol trispyrophosphate (ITPP) is an allosteric effector that increases oxygen unloading by red blood cells (RBCs)[30], leading to increased oxygenation in tumors[31–35]. Furthermore, ITPP may contribute to producing a "hot" tumor by increasing immune cell influx, reducing the frequencies of myeloid and regulatory T cell populations in tumors, and decreasing PD-L1 expression in the tumor[34–36]. A recent clinical trial (NCT02528526) assessing tumor control by ITPP found that 52% of patients treated with ITPP had stable disease and 60% of patients treated with ITPP and subsequent chemotherapy had stable disease[37]. Preclinical studies have tested ITPP as a monotherapy[32,36–42], and in combination chemotherapy[34,43] and radiotherapy[31,35,44] with mixed results. Surprisingly, ITPP has not been tested in combination with ICB such as αPD-1 and αCTLA-4[45,46]. In this study, we take the paradigm of combination therapy with ITPP a step further by postulating that ITPP potentiates ICB tumor response.

To investigate this next-step paradigm, we investigated non-invasive imaging as a tool to monitor HbO_2 in pre-clinical tumor models. Other studies have used EPR imaging to monitor pO2 in the extracellular tumor microenvironment[31–33], MRI to indirectly evaluate oxygenation through water relaxation[32,47], and Bioluminescence imaging and PET to qualitatively assess intracellular hypoxia[35,47]. We elected to use photoacoustic imaging (PAI; also known as multispectral optoacoustic tomography) as a more direct interrogation of the effect of ITPP on HbO_2[48,49]. PAI can measure the relative concentrations of deoxyhemoglobin (Hb) and oxyhemoglobin (HbO_2) based on their signature PA spectral profiles after absorbance of near-infrared light[50,51]. These measurements can be used determine % saturation of oxygen ($\%sO_2 = HbO_2/(HbO_2 + Hb)$), which should decrease when ITPP increases oxygen unloading that converts HbO_2 into Hb. Another study used PAI to evaluate the effects of ITPP as a pre-clinical tumor treatment, but did not report $\%sO_2$ values in synchrony with ITPP treatment[36]. In this study, we postulated that non-invasive tracking of $\%sO_2$ with PAI in synchrony with ITPP treatment can improve our understanding how ITPP may potentiate ICB response.

Results

ITPP sensitized CT26 tumors to ICB

ITPP promoted oxygen unloading in CT26 tumors

We chose CT26 colon carcinoma as our murine model for this test, based in its relative susceptibility to ICB and its well-characterized hypoxic TME[52–54]. Furthermore, CT26 was developed in the albino Balb/cJ background, which is imperative for our studies as PAI is sensitive to melanin.

We tracked the effect of three longitudinal doses of ITPP on $\%sO_2$ to indirectly monitor a decrease in tumor hypoxia and whether the change is durable. PAI was performed three hours after administration of ITPP or PBS as control on Days 12, 15, and 18 (relative to tumor implantation on Day 0), with the comparative pre-ITPP baseline PAI scan taken on Day 11 (Fig. 1a,b). Our results showed a marked decrease in $\%sO_2$ three hours after the first dose of ITPP (Fig. 1c), which reflects oxygen unloading that converts HbO_2 into Hb. This decrease in $\%sO_2$ observed with the first dose of ITPP was not seen with the second or third doses of ITPP, demonstrating that the oxygen unloading by ITPP was not durable in our study.

Oxygen unloading caused by ITPP correlated with increased Teff and decreased monocyte frequencies in CT26 tumors

Because our previous experiment showed a significant decrease in $\%sO_2$ three hours after one dose of ITPP, we were particularly interested in whether this change in $\%sO_2$ was related to the immunogenicity of the tumor as primed by ITPP. To that end, we harvested tumors following PAI that occurred three hours after the first ITPP injection and assessed the immune cell populations by flow cytometry (Fig. 2a). A comparison of the frequencies of immune cell populations in CT26 tumors and $\%sO_2$ after the first ITPP injection showed that ITPP caused tumors to be more immunogenic, or "hot". At lower $\%sO_2$, where oxygen unloading into the tumor TME was greater, we observed greater frequencies of CD8 and CD4 + FoxP3- effector T cells (Teffs) in CT26 tumors (Fig. 2b,c). We also observed a weak correlation between $\%sO_2$ and the frequencies of Ly6C + monocytic myeloid cells (Fig. 2d). Therefore, ITPP primes CT26 tumors to be "hot" for ICB therapy by increasing Teff while decreasing monocytic population frequencies.

Combination ITPP and ICB delayed growth of CT26 tumors

Because ITPP relieves hypoxia and converts CT26 tumors into "hot" immunogenic tumors three hours after the first ITPP injection, we next asked whether the effect of ITPP to create an immunogenically "hot" TME is sufficient to strengthen the ICB response and promote ICB tumor control. As CT26 tumors are more susceptible to ICB therapy[52–54], we allowed CT26 tumors to develop further in diameter to 5–6 mm to enhance tumor resistance to ICB. We treated mice bearing the CT26 tumor model with ITPP followed 3 h later with αCTLA-4 and αPD-1 ICB and performed in 3-day intervals (Fig. 3a). We also tested ITPP only, αCTLA-4 and αPD-1 only, and vehicle as controls in the same 3-day intervals. We monitored the treatment responses by measuring tumor volume and tracking mouse survival.

When compared to the three controls, combination ITPP, αCTLA-4, and αPD-1 significantly reduced CT26 tumor growth and increased survival in this treatment group (Fig. 3b,c). The majority of mice receiving combination treatment rejected their tumors while control treatments showed no tumor rejection (Fig. 3d). While this data shows that ITPP promotes ICB tumor control, it should be noted that ITPP significantly decreased $\%sO_2$ only after the first treatment. Therefore, the initial hypoxic state of the TME may be more consequential in determining ICB tumor response rather than subsequent tumor hypoxic states.

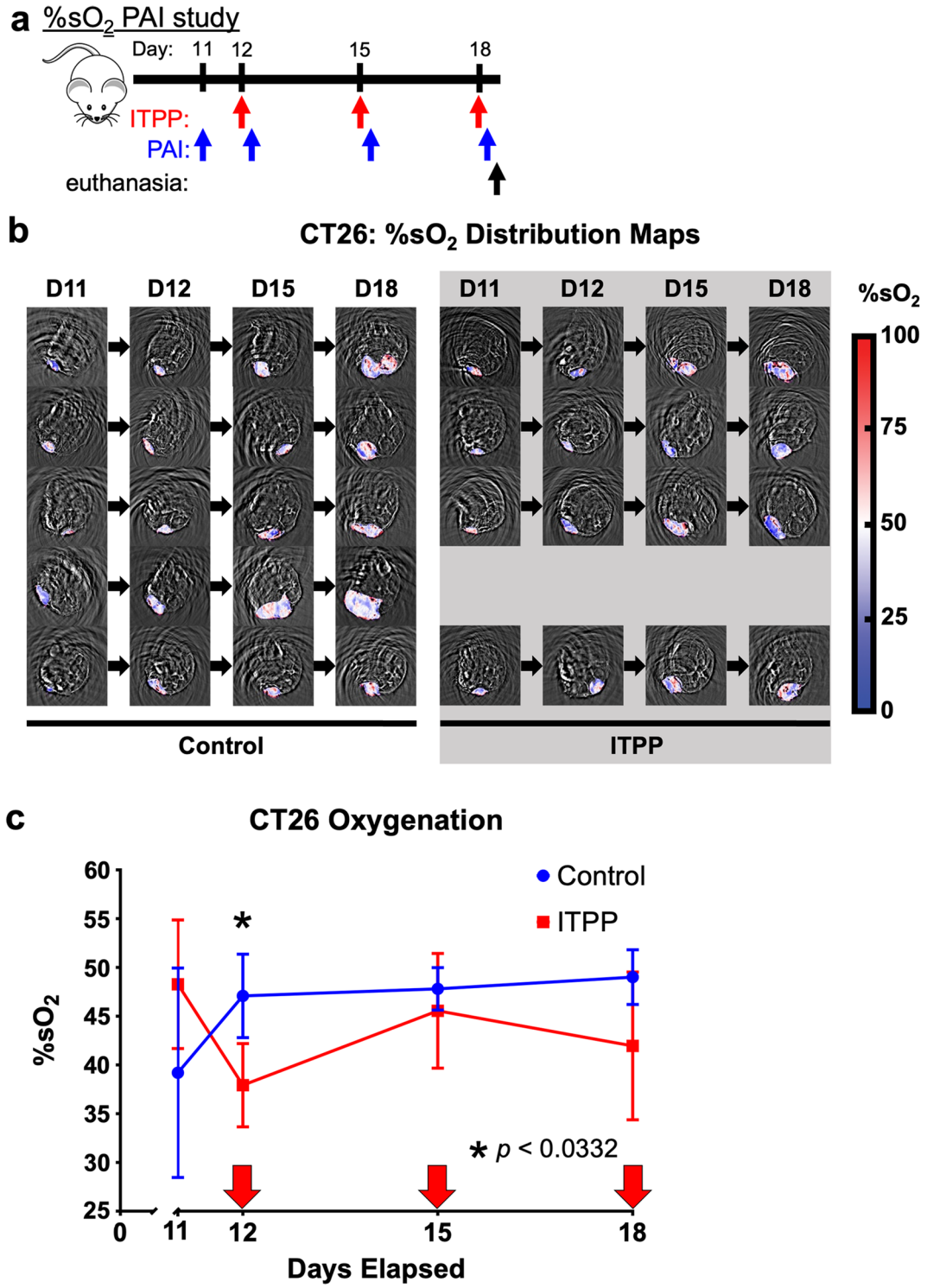

Fig. 1. ITPP increased oxygen delivery to CT26 tumors. (**a**) A study timeline. PAI was performed 3 h after administering ITPP. Mice were euthanized after the PAI scan. (**b**) The $\%sO_2$ distribution maps of CT26 tumors subcutaneously implanted in female Balb/cJ mice, subdivided by treatment. (**c**) The change in $\%sO_2$ throughout the treatment period of the CT26 model receiving PBS control or ITPP treatment. Arrows indicate days when mice received treatment. Values show the average tumor $\%sO_2$ and error bars represent standard deviation. *$p < 0.0332$, $n = 4–5$, field of view 25 × 25 mm.

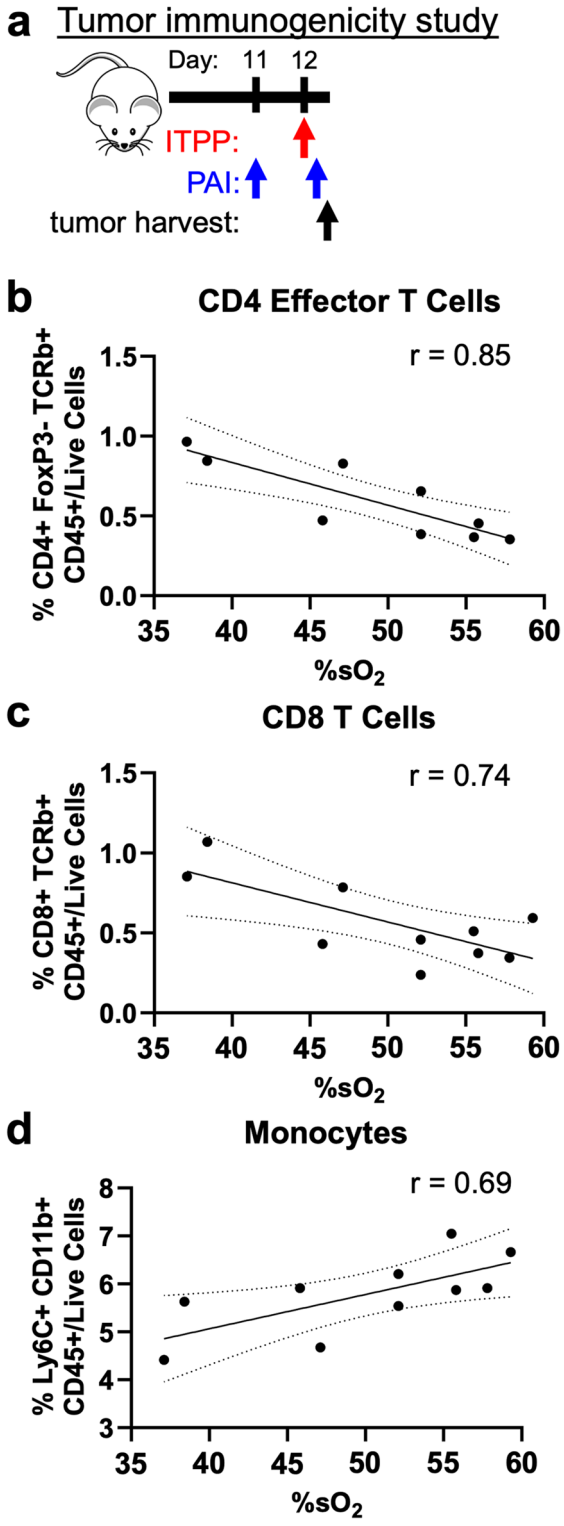

Fig. 2. ITPP improved CT26 tumor immunogenicity. (**a**) A study timeline. ITPP was administered on Day 12, then PAI was performed 3 h later, and then immediately followed by tumor harvest for cell analysis. The correlation between the frequencies of $\%sO_2$ and (**b**) CD4 + FoxP3-TCRb + CD45 + /live cells, (**c**) CD8 + TCRb + CD45 + /live cells, or (**d**) Ly6C + CD11b + CD45 + /live cells in CT26 tumors three hours after the ITPP treatment on Day 12. Dotted lines represent the 95% confidence interval while the solid lines represent the linear best fit line. $n = 9–10$.

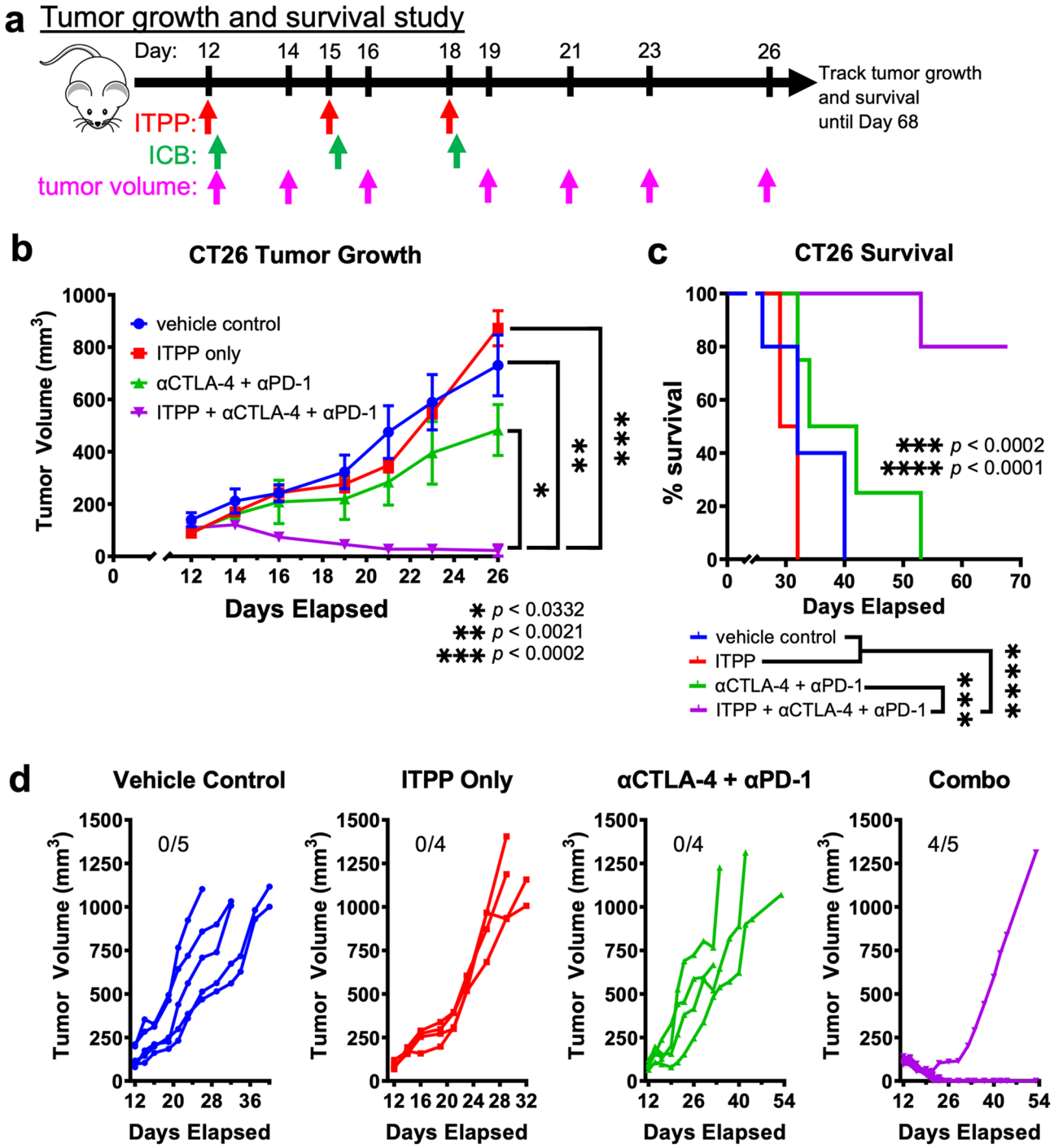

Fig. 3. ITPP promoted ICB rejection of CT26 tumors. (**a**) A study timeline. ICB was administered 3 h after ITPP. (**b**) Tumor growth kinetics and (**c**) survival data of Balb/cJ mice bearing subcutaneously implanted CT26 tumors and receiving the indicated treatments. $^{*}p < 0.0332$, $^{**}p < 0.0021$, $^{***}p < 0.0002$, $^{****}p < 0.0001$. (**d**) Individual tumor growth kinetics within each respective treatment group showing the number of tumors rejected. Values are shown as average, and error bars represent standard error of the mean. $n = 4–5$, with three biological repeats.

ITPP sensitized 4T1 tumors to ICB

ITPP promoted oxygen unloading in 4T1 tumors

Despite the efficacy of ITPP and ICB in the CT26 model, reproducing these results in a more ICB resistant tumor model is necessary to validate our findings. We chose the 4T1 model as it is less susceptible to ICB compared to the CT26 model, which we also developed in the Balb/cJ background[55,56].

We began by assessing oxygen unloading by ITPP in the 4T1 tumors using PAI. Mice bearing orthotopically implanted 4T1 tumors were treated with either ITPP or PBS as control on days 10, 13, and 16, and PAI was conducted on day 9 and three hours after each ITPP treatment (Fig. 4a,b). In a similar manner to the CT26 tumors, ITPP significantly reduced $\%sO_2$ in 4T1 tumors three hours after the first ITPP treatment (Fig. 4c). Unlike the results with CT26 tumors, continued ITPP treatment showed a slow and gradual recovery of $\%sO_2$ in the 4T1 tumors. However, there was no significant difference in tumor $\%sO_2$ between the mice receiving PBS after the second and third injection. Based on these results, ITPP demonstrated the capacity to increase oxygen unloading in 4T1 tumors three hours after the first ITPP treatment.

Oxygen unloading correlated with increased Teff and decreased monocyte frequencies in 4T1 tumors

To assess the efficacy of ITPP for promoting "hot" 4T1 tumors, we harvested 4T1 tumors after PAI three hours following initial ITPP treatment (Fig. 5a). We focused on this timepoint as it was the only timepoint to significantly reduce $\%sO_2$ in the previous experiment (Fig. 4c). Harvested tumors were then processed using flow cytometry to determine the frequencies of immune cell populations in the tumors.

Results from the flow cytometry analysis correlated similarly to those of CT26 tumors. The frequencies of Teff cells in 4T1 tumors increased with lower $\%sO_2$ (Fig. 5b,c). Despite correlating weakly, the frequencies of monocytes in 4T1 tumors also increased at higher $\%sO_2$ (Fig. 5d). As decreased $\%sO_2$ reflects oxygen unloading in tumor vessels, this data indicates that improved oxygenation in the TME increased Teff infiltration and reduced the presence of immunosuppressive monocytes populations in 4T1 tumors, causing the tumors to become immunogenically "hot".

Combination ITPP and ICB delayed growth of 4T1 tumors

Similar to our studies with the CT26 model, we assessed whether the immunogenicity induced by ITPP treatment of 4T1 tumors results in enhanced ICB tumor response. We conducted tumor growth studies combining ITPP and followed 3 h later with αCTLA-4 and αPD-1 and repeated in 3-day intervals. We also tested ITPP only, αCTLA-4 and αPD-1 only, and vehicle as controls (Fig. 6a). We measured tumor and mouse survival as indicators of tumor control. Because previous studies found 4T1 tumors to be more resistant to ICB[55,56], 4T1 tumors were allowed to reach a smaller diameter before initiating treatment (3–4 mm) compared to that of CT26 tumors. Furthermore, we treated 4T1 tumors with four doses of ITPP and/or αCTLA-4 and αPD-1, or vehicle, in three-day intervals, to emphasize the effect of combination ITPP and ICB.

Similar to the results of ITPP and ICB on the CT26 tumor model, the combination of ITPP with αCTLA-4 and αPD-1 significantly delayed 4T1 tumor growth compared to controls (Fig. 6b). The combination treatment also improved survival of mice bearing 4T1 tumors, although this improved survival was not statistically significant when comparing ITPP and ICB vs. ICB alone (Fig. 6c). This improved survival was partly due to a small increase in the frequency of 4T1 tumor rejection (Fig. 6d). For mice to reject some 4T1 tumors after treatment with αCTLA-4 and αPD-1, but not in CT26 tumors, may reflect a difference in tumor susceptibility to ICB for the two models at their respective starting diameters.

The $\%sO_2$ indicated tumor control mediated by combination ITPP and ICB by enhancing frequencies of Teffs and Teff subsets

The $\%sO_2$ of tumors after initial ITPP treatment correlated with combination ITPP and ICB tumor response in CT26 and 4T1 tumors

Because our previous experiments showed that $\%sO_2$ measurements from PAI (Figs. 1 and 4) indicate that ITPP can prime TMEs to be immunogenically "hot" (Figs. 2 and 5), and that ITPP can potentiate ICB tumor control (Figs. 3 and 6), we postulated that PAI measurements on the day of initiating treatment are related to tumor control after ITPP and ICB at a later day. We were also interested in examining whether $\Delta\%sO_2$ is related to tumor control at a later day. The timeline of this study for both tumor models is shown in Fig. 7a,b.

All of the CT26 tumors and the majority of 4T1 tumors had $\Delta\%sO_2$ values less than 0, indicating that ITPP decreased $\%sO_2$ and thus promoted oxygen unloading (Fig. 7c,d). The $\Delta\%sO_2$ of both tumor models bracketing initial treatment was correlated with tumor mass 5 days later. Similarly, post-ITPP $\%sO_2$ in both CT26 and 4T1 tumors was positively correlated with tumor mass after ICB treatment (Fig. 7e,f). The $\Delta\%sO_2$ value is based on two $\%sO_2$ measurements, and therefore may have more experimental variability, which may explain the difference in correlations between Fig. 7c and d. Most importantly, these results indicated that $\Delta\%sO_2$ and $\%sO_2$ measured at the start of treatment are early response biomarkers for our specific studies on the day of treatment that foreshadow eventual tumor control on later days.

$\%sO_2$ after initial ITPP treatment correlates with frequencies of Teffs

As the previous experiment established post-ITPP $\%sO_2$ as an early response biomarker for tumor control in both CT26 and 4T1 tumors in our studies, we sought to determine the cellular mechanism driving the ability of $\%sO_2$ to be related to tumor control by ITPP and ICB. We analyzed the immune infiltrate in CT26 and 4T1 tumors after PAI, and compared our immunophenotyping results to post-ITPP $\%sO_2$ to determine the cellular changes associated with increased oxygen unloading by RBCs in the tumor. The timeline of this study for both tumor models is shown in Fig. 8a,b, which are the same timelines as shown in Fig. 7a,b.

We observed specific correlations when comparing the frequencies of certain immune cell populations in the tumors to post-ITPP $\%sO_2$. Teff frequencies in CT26 and 4T1 tumors negatively correlated with their respective post-ITPP $\%sO_2$ measurements (Fig. 8c and d). These Teff populations were not associated with increased cytotoxic function, however, as the examination of granzyme B expression in Teff cells did not yield a correlation between granzyme B-expressing Teff frequencies and post-ITPP $\%sO_2$ (data not shown). Among the Teff populations, we observed a negative correlation between the frequencies of TCF-1 + Teff and their

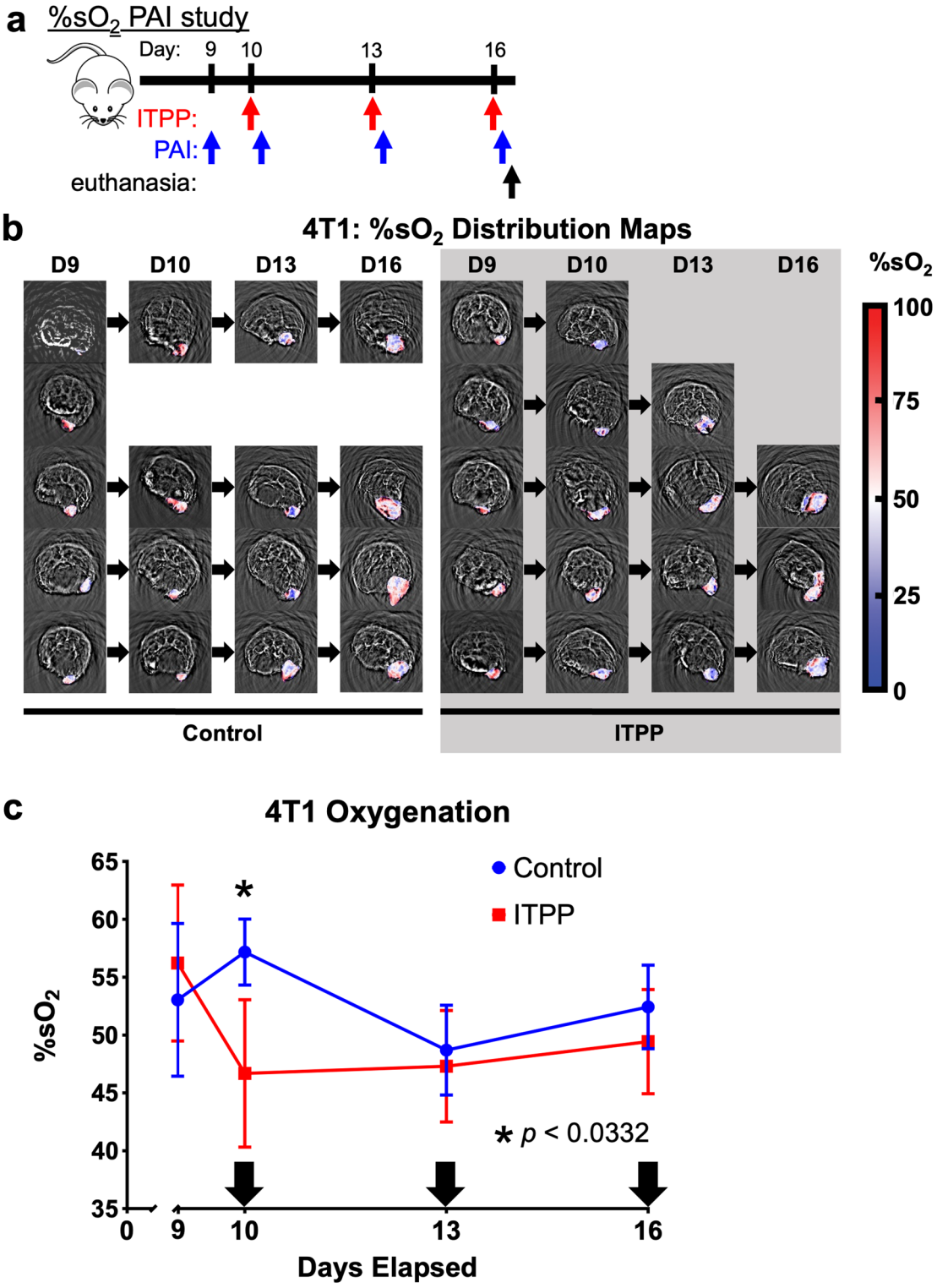

Fig. 4. ITPP increased oxygen delivery to 4T1 tumors. (**a**) A study timeline. PAI was performed 3 h after administering ITPP. Mice were euthanized after the last PAI scan. (**b**) The $\%sO_2$ distribution maps of 4T1 tumors subcutaneously implanted in female Balb/cJ mice, subdivided by treatment. (**c**) The change in $\%sO_2$ throughout the treatment period of the 4T1 model receiving PBS control or ITPP treatment. Arrows indicate days when mice received treatment. Values show the average tumor $\%sO_2$ and error bars represent standard deviation. *$p < 0.0332$, $n = 4–5$, field of view 25 × 25 mm.

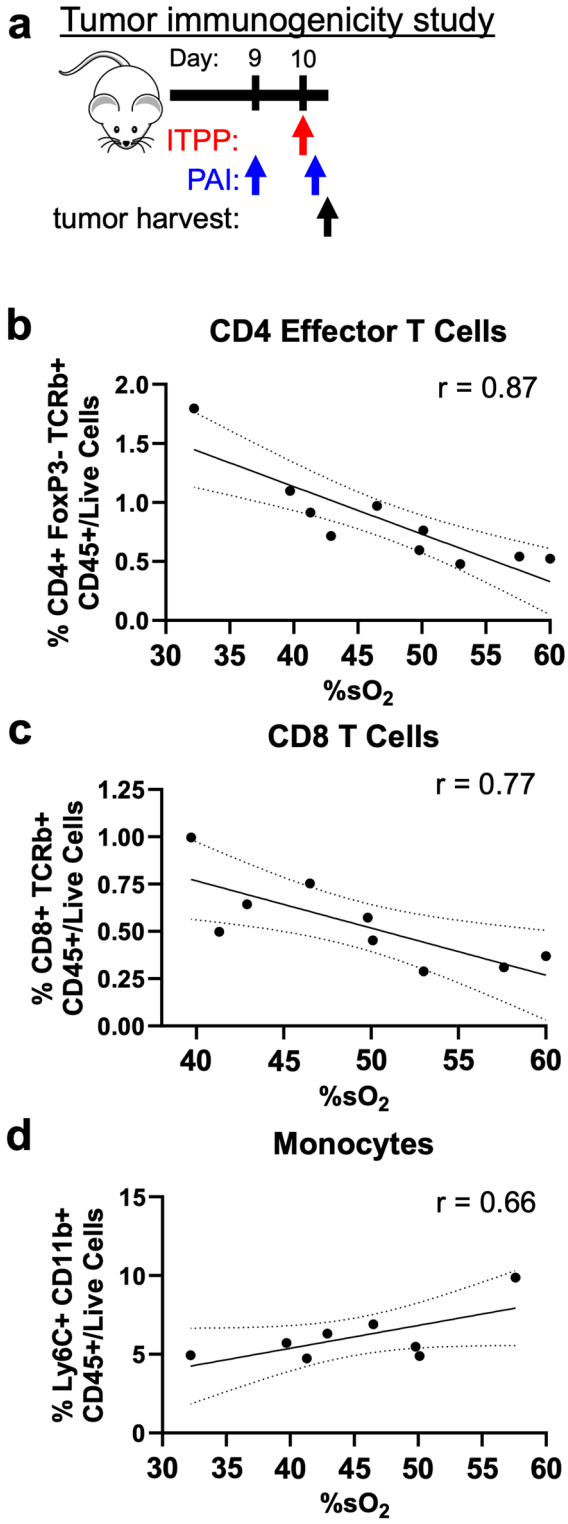

Fig. 5. ITPP improved 4T1 tumor immunogenicity. (**a**) A study timeline. ITPP was administered on Day 10, then PAI was performed 3 h later, and then immediately followed by tumor harvest for cell analysis. The correlation between the frequencies of $\%sO_2$ and A) CD4 + FoxP3-TCRb + CD45 + /live cells, (**b**) CD8 + TCRb + CD45 + /live cells, or (**c**) Ly6C + CD11b + CD45 + /live cells in 4T1 tumors three hours after the ITPP treatment on Day 10. Dotted lines represent the 95% confidence interval while the solid lines represent the linear best fit line. $n = 8–10$.

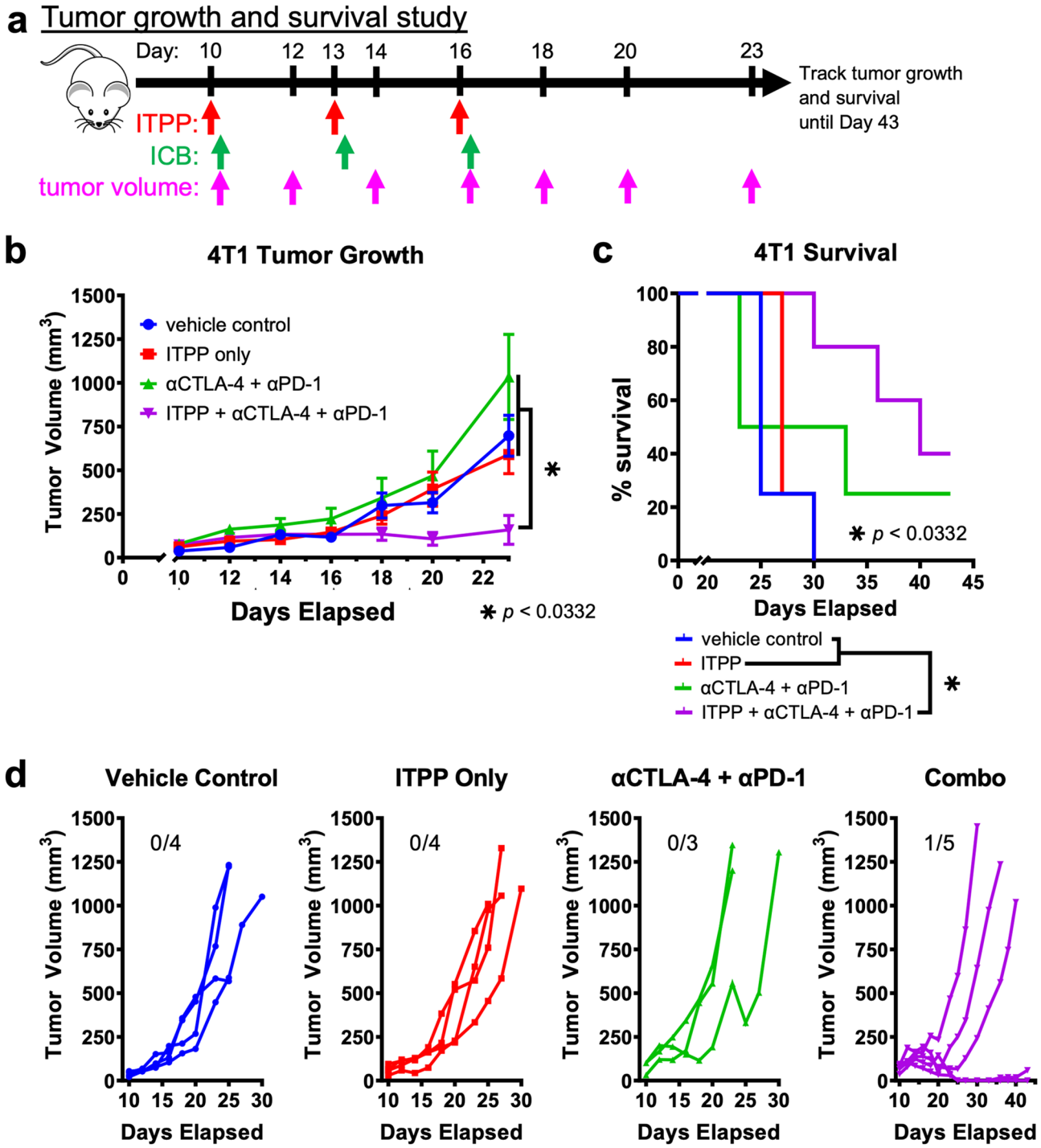

Fig. 6. ITPP promoted ICB control of 4T1 tumors. (**a**) A study timeline. ICB was administered 3 h after ITPP. (**b**) Tumor growth kinetics and (**c**) pooled survival data of Balb/cJ mice bearing orthotopically implanted 4T1 tumors and receiving the indicated treatments. (**d**) Individual tumor growth kinetics within each respective treatment group showing the number of tumors rejected. Values are shown as average, and error bars represent standard error of the mean. $^{*}p < 0.0332$. $n = 4–5$, with three biological repeats.

respective post-ITPP $\%sO_2$ in both CT26 and 4T1 tumors (Fig. 8e and f). Furthermore, TOX + Teff frequencies had a positive correlation with post-ITPP $\%sO_2$ in CT26 and 4T1 tumors (Fig. 8g and h). After assessing the frequencies of different myeloid cell populations as well as the frequencies of stimulatory and inhibitory marker-expressing myeloid populations, there were no significant correlations between any myeloid cell populations and post-ITPP $\%sO_2$ (data not shown).

As TCF-1 is a marker of fit, progenitor T cells[57] whereas TOX is a marker of exhausted T cells[58], our data indicates that decreased $\%sO_2$ after ITPP is associated with less Teff exhaustion in both CT26 and 4T1 models.

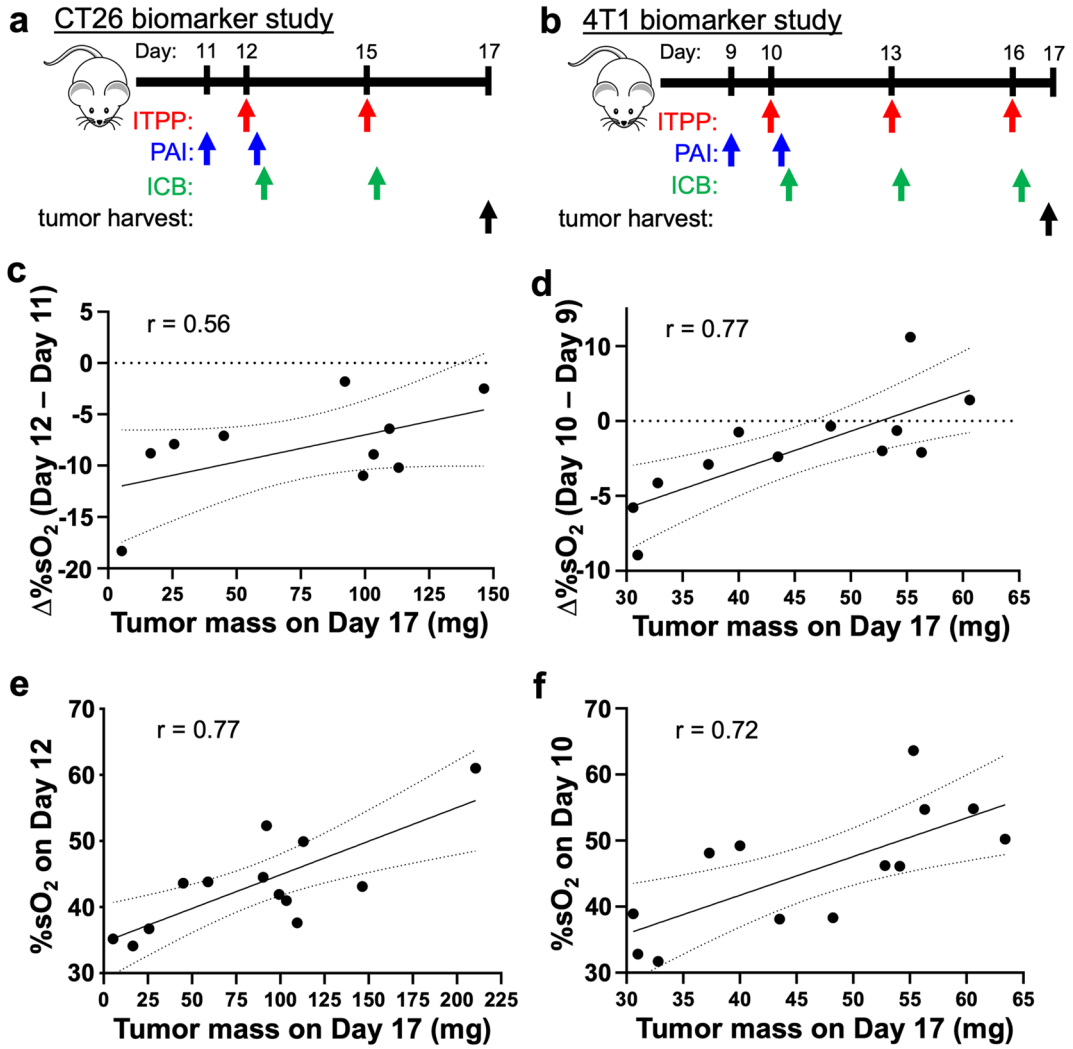

Fig. 7. $\%sO_2$ after the first ITPP treatment positively correlated with combination ITPP and ICB tumor control. (**a,b**) The study timelines. PAI was performed 3 h after administering ITPP. ICB was administered immediately after PAI on the initial treatment day. ICB was administered 3 h after ITPP on days without PAI. The comparison between the change in $\%sO_2$ ($\Delta\%sO_2$) three hours after initial ITPP treatment relative to pretreatment, compared to the mass of **c**) CT26 and (**d**) 4T1 tumors after two combination ITPP, αCTLA-4 and αPD-1 treatments. A similar comparison between $\%sO_2$ three hours after initial ITPP treatment and the mass of (**e**) CT26 and **f**) 4T1 tumors after two combination treatments. Dotted lines represent the 95% confidence interval while the solid lines represent the linear best fit line. $n = 10–13$.

Because post-ITPP $\%sO_2$ positively correlates with tumor mass, increased Teffs, TCF-1 + Teffs, and decreased TOX + Teffs are also associated with low tumor mass following ITPP and ICB treatment. While these Teff populations are not more cytolytic, a more pronounced infiltration of these T cells can increase their antitumor effect by sheer volume. Therefore, more TCF-1 + Teffs and fewer TOX + Teffs in tumors mediate the tumor control induced by ITPP, αCTLA-4 and αPD-1. Low post-ITPP $\%sO_2$ can therefore be an early response biomarker in our studies of combination ITPP and αCTLA-4 and αPD-1 efficacy as well as an indicator for increased progenitor Teff infiltration.

Discussion

Our work showed that ITPP increases oxygen unloading from hemoglobin, leading to increased tumor immunogenicity and synergy with ICB, and was related to tumor control by combination ITPP and ICB in the CT26 and 4T1 tumor models. Low $\%sO_2$ induced by ITPP promotes the conversion of CT26 and 4T1 into "hot" tumors by increasing the frequencies of Teffs, while decreasing the frequencies of monocytes in the tumors. Combination treatment of ITPP, αCTLA-4 and αPD-1 significantly delayed tumor growth in both CT26 and 4T1 models in a manner related to low post-ITPP $\%sO_2$. Lastly, low post-ITPP $\%sO_2$ was associated with increased frequencies of Teffs, as well as TCF-1 + Teffs, and associated with decreased frequencies of TOX + Teffs. Teff infiltration as well as progenitor, non-exhausted Teff subsets contributed to the antitumor effect of combination therapy ITPP, αCTLA-4 and αPD-1.

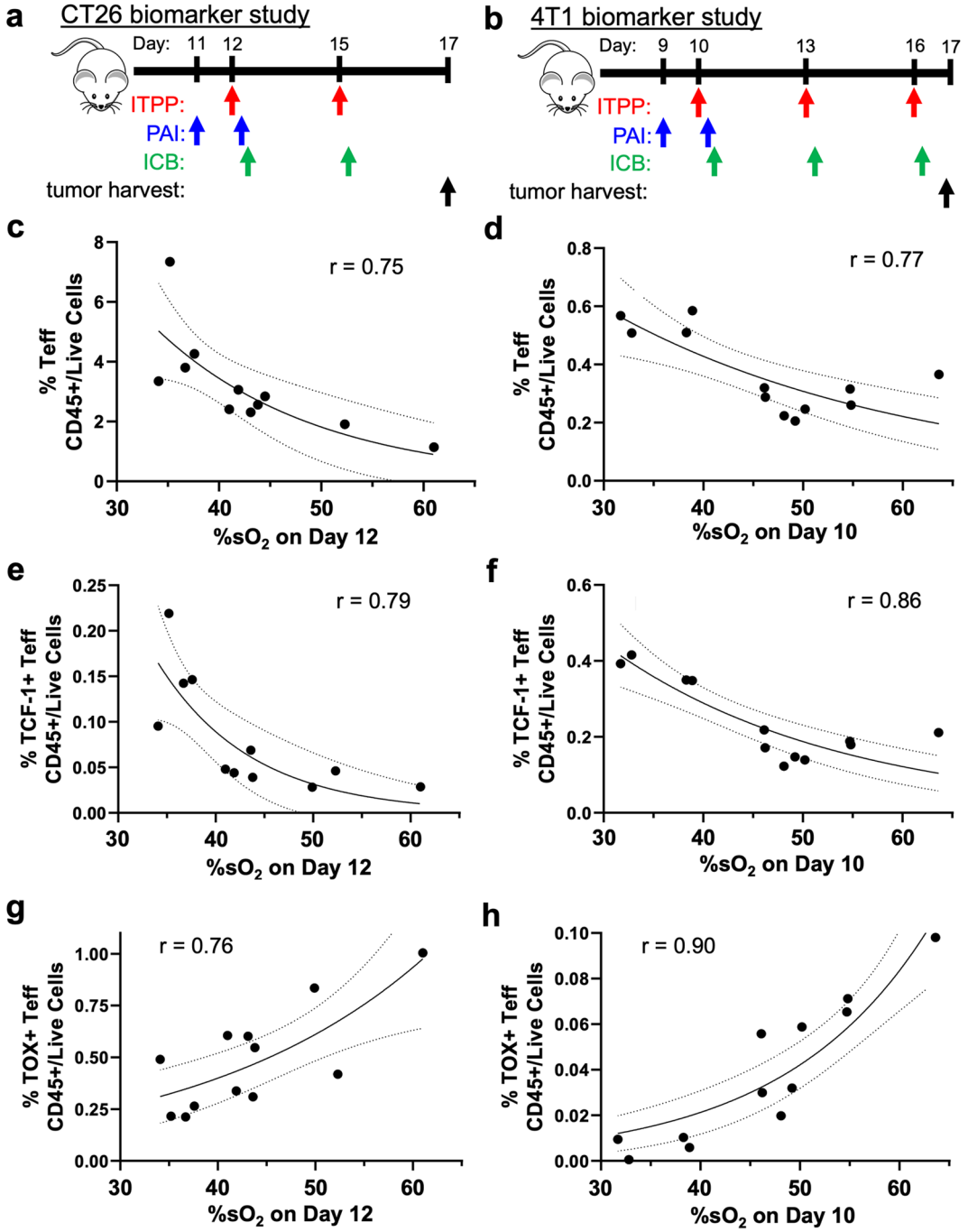

Fig. 8. $\%sO_2$ after the first ITPP treatment correlated with intratumoral frequencies of Teffs following ITPP and ICB treatment. (**a**,**b**) The study timelines. PAI was performed 3 h after administering ITPP. ICB was administered immediately after PAI on the initial treatment day. ICB was administered 3 h after ITPP on days without PAI. Negative correlations between $\%sO_2$ three hours after ITPP and the frequencies of (**c**) CD8 and CD4 + FoxP3- T cells in CT26 tumors, (**d**) CD8 and CD4 + FoxP3- 4T1 tumors, (**e**) TCF-1 + CD8 and TCF-1 + CD4 + FoxP3- T cells in CT26 tumors, and (**f**) TCF-1 + cD8 and TCF-1 + CD4 + FoxP3- T cells in 4T1 tumors after two or three commination ITPP, αCTLA-4 and αPD-1 treatments. Positive correlations between $\%sO_2$ three hours after ITPP and the frequencies of TOX + CD8 and TOX + CD4 + FoxP3- T cells in (**g**) CT26 and (**h**) 4T1 tumors after ITPP, αCTLA-4 and αPD-1 treatments. Dotted lines represent the 95% confidence interval while the solid lines represent the linear best fit line. $n = 11–12$.

Both tumor models had a similar modulation of the immune cell composition in response to ITPP. Both CT26 and 4T1 tumors increased their frequencies of Teff cells at low $\%sO_2$ induced by ITPP (Fig. 2b,c, 5b,c), which carried over to the response to combination ITPP, αCTLA-4 and αPD-1 (Fig. 8c,d). Our results with our models of breast and colon cancers are similar to previous studies that showed elevated immune cell influx into

tumors of rat and mouse models of head and neck, lung, colon, and pancreatic cancers[34–36]. However, more studies with additional tumor models are needed to investigate whether the conversion of immunogenically "cold" tumors into "hot" tumors that have high T cell penetrance is a common feature of all cancer types[1,25]. In particular, while CT26 and 4T1 are considered to be moderately hypoxic tumors[59,60], both normoxic and highly hypoxic tumor models should be considered. Most importantly, we have performed the first study that combines ITPP with ICB. Additional pre-clinical studies that use ITPP to convert "cold" tumors into "hot" tumors should also include ICB treatment.

Our results showed that ITPP only produced a significant change in $\%sO_2$ three hours after the first treatment, but not after the second and third treatments (Figs. 1c and 4c). This result showed the value of in vivo imaging to monitor longitudinal changes in tumor models, especially because we assumed that a sustained change in $\%sO_2$ would occur after each ITPP treatment. Future studies can evaluate other longitudinal doses and timings of ITPP and ICB that may elucidate the longitudinal pharmacodynamics of combination treatments. Other agents that promote oxygenation in the TME can also be studied using longitudinal PAI studies. For example, PAI has been used to detect the release of O_2 from hemoglobin by an analog of sulfoquinovosylacylglycerol[61] and also detected the production of O_2 by metallic nanoparticles[62,63]. Future studies could also use PAI to image an untreated control group or a group only treated with ICB, although no change in $\%sO_2$ would be expected.

Our study indicates that further technical improvements are warranted for evaluating tumor $\%sO_2$ with PAI. For example, the mechanism of ITPP should unload oxygen in more hypoxic tumor regions and reduce the heterogeneity of oxygen distribution within the tumors. We only analyzed the average tumor $\%sO_2$ due to PAI measurement imprecision, rather than analyzing pixelwise values of $\%sO_2$. Also, our methodology only analyzed one imaging slice through the tumor. A more precise imaging method and/or multislice imaging to analyze the entire tumor may provide opportunities to evaluate $\%sO_2$ heterogeneity as a complementary biomarker [e.g., replacing $\%sO_2$ with a '$\%sO_2$ heterogeneity' biomarker in Figs. 2, 5, 7, and 8). We did not evaluate total hemoglobin (HbT) in our study despite measuring Hb and HbO_2 (where $HbT = Hb + HbO_2$) because light scattering and absorption in tissues can influence HbT measurements at different tissue depths[64]. The ratiometric measurement of $\%sO_2$ mitigates this effect, making $\%sO_2$ a more reliable parameter[65]. Yet, accounting for light scattering and absorption in future PAI studies may lead to evaluations of HbT and may also improve the precision of $\%sO_2$ measurements[66].

We used $\%sO_2$ measurements with PAI to verify the mechanism of ITPP-mediated release of O_2 from HbO_2 in vivo. However, PAI cannot directly measure oxygenation in the TME, which is important for studies of immunotherapy studies because immune cells interact with tumor cells within the TME. For comparison, EPR imaging and MRI can directly evaluate pO_2 in the TME and have been used to confirm that ITPP increases pO_2 in the TME[31–33]. However, EPR imaging and MRI cannot confirm the mechanism of ITPP-mediated release of O_2 from HbO_2. Therefore, the combination of these previous reports and our study strengthen our understanding of how ITPP potentiates ICB.

Oxygenation of the TME can also be improved by increasing tumor vascular perfusion[67]. Previous studies showed the capacity of ITPP to normalize vasculature and promote tissue perfusion[68]. We have invented a method that can quantitatively measure the tumor vascular perfusion rates in tumor models, known as Dynamic Contrast Enhanced (DCE) PAI[69], which can be performed with $\%sO_2$ PAI during a single scan session[70]. Future studies can use a combination of $\%sO_2$ PAI and DCE PAI for pre-clinical investigations of ITPP with ICB. For comparison, EPR imaging, bioluminescence imaging, PET and MRI have also been used to evaluate the tumor response to ITPP[31–33,35,47]. However, EPR imaging and bioluminescence imaging cannot measure vascular perfusion, and DCE PET is rarely employed due to poor spatial resolution. DCE MRI has many technical limitations[71–73] and is often relegated to qualitative contrast-enhanced MRI that cannot measure vascular perfusion rates[74,75]. Therefore, the combined methodology of $\%sO_2$ PAI and DCE PAI is a new paradigm for imaging the effects anti-cancer therapies in pre-clinical tumor models. Furthermore, $\%sO_2$ PAI is now approved for imaging breast cancer[76], and we are translating DCE PAI to clinical practice. A combined protocol for $\%sO_2$ PAI and DCE PAI may eventually benefit clinical treatment studies, and may aid in stratifying patients into treatment groups that would or would not benefit from combination treatments that improve tumor oxygenation prior to ICB.

Methods

ITPP

We synthesized ITPP with a Na^+ counterion based on a published procedure[78,79]. The sodium salt of phytic acid (Themofisher, Inc.) was acidified by Dowex H^+ resin (Sigma–Aldrich). Triethylamine was used to protect the acid. 1,3-dicyclohexylcarbodiimide (8 eq, Sigma–Aldrich) dissolved in acetonitrile was added to the water solution of the triethylamine protected compound and refluxed overnight. After dilution with ddH_2O, the solid formed was vacuum filtered away. The pass-through liquid was lyophilized to dryness. Dowex Na form resin (Sigma–Aldrich) was used to ionize the dissolved water solution from the previous step to sodium form. The reaction crude was purified by HPLC (1% to 30% acetonitrile in water gradient). 1H NMR (D2O, 600 MHz): 4.43 (s, 6H). C NMR (D2O, 600 MHz): 75.64 (s): 'P NMR (D2O, 300 MHz): – 9.2536. (ESI): *m/z* Calcd for C6H12O21P6 [M^+]: 605.98, Found: 607.03. [M^-]: 604.98, Found:604.85.

To prepare ITPP for in vivo studies described below, ITPP was dissolved in sterile phosphate-buffered saline (PBS) for a final concentration of 22.22 g/mL. The ITPP solution was then passed through a 0.22 µm filter followed by processing using an endotoxin removal kit (Thermo Scientific, 88276). ITPP was injected intraperitoneally at a dose of 2.222 g/kg.

Antibodies

To prepare antibodies for in vivo studies described below, the αCTLA-4 (9H10) and αPD-1 (RMP1-14) antibodies (Leinco Technologies, C2841 and P372, respectively) were diluted in PBS and injected intraperitoneally at doses of 5 mg/kg and 12.5 mg/kg, respectively. PBS was injected intraperitoneally as the vehicle control.

Cell lines

To prepare tumor models for in vivo studies described below, CT26 murine colon carcinoma cells (ATCC, CRL-2638) were grown in Roswell Park Memorial Institute 1640 (RPMI) media supplemented with 10% FBS, 2% penicillin and streptomycin, 1% L-glutamine, and 1% sodium pyruvate in tissue culture-treated flasks. 4T1 murine mammary epithelial cells (CVCL_0125, ATCC, CRL-2539) derived from female mice were also grown in tissue culture-treated flasks supplemented with RPMI and additional 10% FBS, 1% penicillin and streptomycin, and 1% L-glutamate, but lacking HEPES and sodium pyruvate. No testing was done on these cell lines because the cell bank ATCC uses the Promega PowerPlex 18D System to identify cell lines by Short Tandem Repeat analyses. Cells were manipulated upon reaching 90% confluence prior to twenty passages. CT26 and 4T1 tumor cell lines were initially selected due to their sensitivity to combination αPD-1 and αCTLA-4 treatment without complete tumor rejection[52–56].

Pre-clinical tumor models and treatments

All experiments involving mice were performed in accordance with the relevant guidelines and regulations and were conducted according to the protocol number 00001779-RN01 approved by the Institutional Animal Care and Use Committee at the UT MD Anderson Cancer Center. Furthermore, all studies with mice were performed in accordance with the 10 essential items of the ARRIVE guidelines. Female BALB/cJ (IMSR_JAX:000651) mice were purchased from the Jackson Laboratory and housed in a pathogen-free facility fully accredited by the Association for Assessment and Accreditation of Laboratory Animal Care. Mice were initially 6–8 weeks old and approximately 20 g in weight. To develop the CT26 model, 1 million cells were resuspended in 200 µL PBS injected intradermally into the right flank. To develop the 4T1 model, 40,000 cells were resuspended in 50 µL PBS and injected into the fat pad of the 4th inguinal nipple. All cells were implanted in mice between the ages of 5–8 weeks and at least 20 g in weight. Tumor volumes were approximated by measuring the longest diameter (a) and the orthogonal diameter (b) using digital calipers and calculating $a^2b/2$. Mice were randomly selected for each cohort. Each mouse was humanely euthanized using CO_2 inhalation or isoflurane anesthetic overdose followed by cervical dislocation as a secondary method.

Treatment with ITPP began when CT26 tumors reached 5–6 mm in diameter at Day 12, and when 4T1 tumors reached 3–4 mm in diameter on Day 10. Mice were excluded from the study if their tumors were not visible or exceeded 200 mm^3 upon blind distribution prior to the first treatment. The timelines of our $\%sO_2$ PAI studies (Figs. 1 and 4), immunogenicity studies (Figs. 2 and 5), tumor growth and survival studies (Figs. 3 and 6), and biomarker studies (Figs. 7 and 8) are shown in each figure.

For PAI studies, 10 mice of each tumor model were used, with 5 mice tested with ITPP and 5 tested with control. One mouse with a CT26 tumor in the ITPP treatment group expired prior to the first imaging scan (Fig. 1). Three mice with a 4T1 tumor expired before the last imaging scan (Fig. 4). A total of 20 mice were used for immunogenicity studies. For tumor growth and survival evaluations, 60 mice of each tumor model were used, randomly distributed among four treatment tests that were conducted in triplicate, with 5 mice per group. In addition, 26 mice were used for biomarker experiments. Sample sizes ranged from 4 to 12 mice, with tumor growth kinetics and survival studies conducted in triplicate. The range of sample sizes reflected occasional sample losses or unreliable results during biomarker studies that were excluded from the final analysis which ensures that the reported results are rigorous.

Photoacoustic imaging

To perform PAI, a mouse was first anesthetized with 2–5% isoflurane in 21% oxygen breathing gas. The mouse was then secured to a cradle with a snorkel nosecone and placed in an inVision instrument (iThera Medical GmbH, inVision 256-TF), immersed in a tank containing deionized water (Millipore Milli-Q Ultrapure water system, Millipore Sigma, Burlington, MA) pre-heated to 36 °C. This bath temperature allowed anesthetized mice to maintain a body temperature of 37 °C as monitored with a rectal temperature sensor (SA Instruments, Inc., Stony Brook, MA) in preliminary imaging feasibility studies prior to treatment studies. The mouse was allowed to equilibrate to temperature and establish a consistent breathing rate for 12 min, which contributed to consistently high image quality. During this equilibration period, an anatomical ultrasound localizer scan was acquired with 31 contiguous image slices, each with 1 mm thickness, collected around the expected location of the tumor using 800 nm absorbance and 5 averages, which took ~ 4 min to acquire.

To evaluate $\%sO_2$, PA images were acquired for 1 slice centered on the tumor. A B-mode ultrasound image was acquired, which was used to identify the region-of-interest that represented the tumor in the image sets. Using an OPO laser in the inVision instrument to produce a surface fluence of 20 mJ/cm^2, we acquired images with 5 wavelengths at 700, 730, 760, 800, and 850 nm, using 6 averages at each wavelength, and repeated 40 times at 10 Hz laser repetition rate, for a scan time of 2.0 min. Each image was reconstructed using a back-projection method, and each image set was spectrally unmixed via linear regression to generate parametric maps of oxy- and deoxy-hemoglobin, which were used to produce maps of $\%sO_2$ using viewMSOT v 4.0 (iThera Medical). The $\%sO_2$ values of the pixels were averaged for all tumor pixels within the region of interest representing the tumor, where the tumor region was identified in the B-mode ultrasound images. The temporal profiles of each biomarker were evaluated to ensure that results were consistent over the 2-min acquisition, and the average over all time points was determined for each biomarker.

Ex vivo tumor cell analysis

Tumors harvested for flow cytometry were minced and digested for 30 min at 37 °C in RPMI supplemented with Collagenase H (Sigma-Aldrich, 11074059001) and DNAse (Roche, 4716728001). After digestion, tumor samples were mashed against 70 μm cell strainers (Corning Life Sciences, 352350) using the textured end of a 1 mL syringe plunger. Once a single cell solution was produced, the samples were normalized by cell count before being stained with an extracellular antibody cocktail and a UV viability dye (Invitrogen, L34961). Cells were then fixed using a fixation buffer (eBioscience, 00-5523-00). After fixing cells, they were stained intracellularly according to the instructions provided with each antibody. Antibodies included CD45 (BD Biosciences, 748371), CD4 (BioLegend, 100548), CD8 (BioLegend, 100734), Ly6G (BD Biosciences, 563979), F4/80 (BioLegend, 123141), CD11c (BioLegend, 117306), CD11b (BioLegend, 101254), Ly6C (BioLegend, 128026), FoxP3 (BioLegend, 320008), TOX (eBioscience, 12-6502-8), TCF-1 (BD Biosciences, 566693). Flow cytometry was performed with the gating strategy used in Reference 9.

Statistics

Tumor growth and survival experiments used three biological repeats for data analysis. Oxygenation results are presented as mean ± standard deviation, while tumor growth results are presented as mean ± standard error of the mean. All statistical analyses were conducted through GraphPad Prism 9.0.0. The *p*-values and significance were determined by one-way ANOVA. Correlation studies were analyzed using Linear and Exponential Regressions to determine goodness of fit and 95% confidence intervals. No blinding or masking of the identity of the samples or mice was performed during the analyses.

Data availability

All data is available upon request by contacting the corresponding author.

Received: 19 March 2025; Accepted: 5 June 2025
Published online: 01 July 2025

References

1. Sharma, P. & Allison, J. P. Immune checkpoint targeting in cancer therapy: Toward combination strategies with curative potential. *Cell* **161**, 205–214 (2015).
3. Herbst, R. S. et al. Pembrolizumab versus docetaxel for previously treated, pd-l1-positive, advanced non-small-cell lung cancer (KEYNOTE-010): A randomised controlled trial. *Lancet* **387**, 1540–1550 (2016).
4. Reck, M. et al. Five-year outcomes with pembrolizumab versus chemotherapy for metastatic non-small-cell lung cancer with pd-l1 tumor proportion score >/= 50. *J. Clin. Oncol.* **39**, 2339–2349 (2021).
5. Casak, S. J. et al. FDA approvalsummary: Atezolizumab plus bevacizumab for the treatment ofpatients with advanced unresectable or metastatic hepatocellularcarcinoma. *Clin. Cancer Res.* **27**, 1836–1841 (2021).
6. Kantoff, P. W. et al. Sipuleucel-T immunotherapy for castration-resistant prostate cancer. *N Engl. J. Med.* **363**, 411–422 (2010).
7. Motzer, R. J. et al. Adjuvant nivolumab plus ipilimumab versus placebo for localised renal cell carcinoma after nephrectomy (CheckMate 914): A double-blind, randomised, phase 3 trial. *Lancet* **401** (10379), 821–832 (2023).
8. Marabelle, A. et al. Efficacy of pembrolizumab in patients with noncolorectal high microsatellite instability/mismatch repair deficient cancer: Results from the phase II KEYNOTE-158 study. *J. Clin. Oncol.* **1**, 1–10 (2020).
9. Eskander, R. N. et al. Pembrolizumab plus chemotherapy in advanced endometrial cancer. *N Engl. J. Med.* **388**, 2159–2170 (2023).
9. Bajorin, D. F. et al. Adjuvant nivolumab versus placebo in muscle-invasive urothelial carcinoma. *N Engl. J. Med.* **384**(22), 2102–2114 (2021).
10. Hodi, F. S. et al. Nivolumab plus ipilimumab or nivolumab alone versus ipilimumab alone in advanced melanoma (CheckMate 067): 4-year outcomes of a multicentre, randomised, phase 3 trial. *Lancet Oncol.* **19**, 1480–1492 (2018).
11. Hellmann, M. D. et al. Nivolumab plus ipilimumab in advanced non-small-cell lung cancer. *N Engl. J. Med.* **381**, 2020–2031 (2019).
12. Motzer, R. J. et al. Nivolumab plus ipilimumab versus Sunitinib in advanced renal-cell carcinoma. *N Engl. J. Med.* **378**, 1277–1290 (2018).
13. Dowling, C. M. et al. Multiple screening approaches reveal HDAC6 as a novel regulator of glycolytic metabolism in triple-negative breast cancer. *Sci. Adv.* **7**, eabc4897 (2021).
14. Adams, S. et al. A multicenter phase II trial of ipilimumab and nivolumab in unresectable or metastatic metaplastic breast cancer: Cohort 36 of dual anti-CTLA-4 and anti-PD-1 Blockade in rare tumors (DART, SWOG S1609). *Clin. Cancer Res.* **28**, 271–278 (2022).
15. Jayaprakash, P., Vignali, P. D. A., Delgoffe, G. M. & Curran, M. A. Hypoxia reduction sensitizes refractory cancers to immunotherapy. *Annu. Rev. Med.* **73**, 251–265 (2022).
16. Corzo, C. A. et al. HIF-1α regulates function and differentiation of myeloid-derived suppressor cells in the tumor microenvironment. *J. Exp. Med.* **207**, 2439–2453 (2010).
17. Chiu, D. K. et al. Hypoxia induces myeloid-derived suppressor cell recruitment to hepatocellular carcinoma through chemokine (C-C motif) ligand 26. *Hepatology* **64**, 797–813 (2016).
18. Huang, L. E., Arany, Z., Livingston, D. M. & Bunn, H. F. Activation of hypoxia-inducible transcription factor depends primarily upon redox-sensitive stabilization of its alpha subunit. *J. Biol. Chem.* **271**, 32253–32259 (1996).
19. Noman, M. Z. et al. PD-L1 is a novel direct target of HIF-1α, and its Blockade under hypoxia enhanced MDSC-mediated T cell activation. *J. Exp. Med.* **211**, 781–790 (2014).
20. Ruf, M., Moch, H. & Schraml, P. PD-L1 expression is regulated by hypoxia inducible factor in clear cell renal cell carcinoma. *Int. J. Cancer*. **139**, 396–403 (2016).
21. Jayaprakash, P. et al. Targeted hypoxia reduction restores T cell infiltration and sensitizes prostate cancer to immunotherapy. *J. Clin. Invest.* **128**, 5137–5149 (2018).
22. Nakagawa, Y. et al. Effects of extracellular pH and hypoxia on the function and development of antigen-specific cytotoxic T lymphocytes. *Immunol. Lett.* **167**, 72–86 (2015).
23. Kim, H. et al. Engineering human tumor-specific cytotoxic T cells to function in a hypoxic environment. *Mol. Ther.* **16**, 599–606 (2008).
24. Ager, C. R. et al. High potency STING agonists engage unique myeloid pathways to reverse pancreatic cancer immune privilege. *J. Immunother Cancer*. **9**, e003246 (2021).
25. Scharping, N. E., Menk, A. V., Whetstone, R. D., Zeng, X. & Delgoffe, G. M. Efficacy of PD-1 Blockade is peotentiated by metformin-induced reduction of tumor hypoxia. *Cancer Immunol. Res.* **5**, 9–16 (2017).

26. Rodriguez-Berriguete, G. et al. Antitumour effect of the mitochondrial complex III inhibitor Atovaquone in combination with anti-PD-L1 therapy in mouse cancer models. *Cell. Death Dis.* **15**, 32 (2024).
27. Hatfield, S. et al. Immunological mechanisms of the antitumor effects of supplemental oxygenation. *Sci. Transl Med.* **7**, 277ra30 (2015).
28. Moan, N. L. et al. Abstract 4726A: The oxygen carrier Omx restores antitumor immunity and cures tumors as a single agent or in combination with checkpoint inhibitors in an intracranial glioblastoma mouse model. *Cancer Res.* **78**, 4726A–A (2018).
29. Duarte, C. D., Greferath, R., Nicolau, C. & Lehn, J. M. myo-Inositol trispyrophosphate: A novel allosteric effector of hemoglobin with high permeation selectivity across the red blood cell plasma membrane. *ChemBioChem* **11**, 2543–2548 (2010).
30. Tran, L. B. A. et al. Impact of myo-inositol tripyrophosphate (ITPP) on tumour oxygenation and response to irradiation in rodent tumour models. *J. Cell. Molec Med.* **23**, 1908–1916 (2019).
31. Cao-Pham, T. T. et al. Combined endogenous MR biomarkers to assess changes in tumor oxygenation induced by an allosteric effector of hemoglobin. *NMR Biomed.* **33**, e4181 (2020).
32. Krzykawska-Serda, M. et al. Oxygen therapeutic window induced by *myo*-inositol trispyrophosphate (ITPP)-Local pO_2 study in murine tumors. *PLOS One*. **18**, e0285318 (2023).
33. Raykov, Z. et al. Myo-inositol trispyrophosphate-mediated hypoxia reversion controls pancreatic cancer in rodents and enhances gemcitabine efficacy. *Int. J. Cancer*. **134**, 2572–2582 (2014).
34. Grgic, I. et al. Tumor oxygenation by myo-inositol trispyrophosphate enhances radiation response. *Int. J. Rad Oncol. Biol. Phys.* **110**, 1222–1233 (2021).
35. El Hafny-Rahbi, B. et al. Tumour angiogenesis normalized by myo-inositol trispyrophosphate alleviates hypoxia in the microenvironment and promotes antitumor immune response. *J. Cell. Mol. Med.* **25**, 3284–3299 (2021).
36. Schneider, M. A. et al. Phase Ib dose-escalation study of the hypoxia-modifier myo-inositol trispyrophosphate in patients with hepatopancreatobiliary tumors. *Nat. Commun.* **12**, 3807 (2021).
37. Limani, P. et al. The allosteric hemoglobin effector ITPP inhibits metastatic colon cancer in mice. *Annals Surg.* **266**, 746–753 (2017).
38. Förnvik, K., Zolfaghari, S., Saiford, L. G. & Redebrandt, H. N. ITPP treatment of RG2 glioblastoma in a rat model. *Anticancer Res.* **36**, 5751–5755 (2016).
39. Derbal-Wolfrom, L. et al. Increasing the oxygen load by treatment with myo-inositol trispyrophosphate reduces growth of colon cancer and modulates the intestine homeobox gene Cdx2. *Oncogene* **32**, 4313–4318 (2013).
40. Ignat, M. et al. Development of a methodology for in vivo follow-up of hepatocellular carcinoma in hepatocyte specific *Trim24*-null mice treated with myo-inositol trispyrophosphate. *J. Exp. Clin. Cancer Res.* **35**, 155 (2016).
41. Aprahamian, M. et al. *Myo*-Inositoltrispyrophosphate treatment leads to HIF-1α suppression and eradication of early hepatoma tumors in rats. *ChemBioChem* **12**, 777–783 (2011).
42. Limani, P. et al. Antihypoxic potentiation of standard therapy for experimental colorectal liver metastasis through myo-inositol trispyrophosphate. *Clin. Cancer Res.* **22**, 5887–5897 (2016).
43. Iyengar, S. & Schwartz, D. Failure of inositol trispyrophosphate to enhance highly effective radiotherapy of GL261 glioblastoma in mice. *Anticancer Res.* **37**, 1121–1125 (2017).
44. Curran, M. A., Montalvo, W., Yagita, H. & Allison, J. P. PD-1 and CTLA-4 combination Blockade expands infiltrating T cells and reduces regulatory T and myeloid cells within B16 melanoma tumors. *Proc. Natl. Acad. Sci. USA*. **107**, 4275–4280 (2010).
45. Wei, S. C. et al. Distinct cellular mechanisms underlie anti-CTLA-4 and anti-PD-1 checkpoint Blockade. *Cell* **170**, 1120–33e17 (2017).
46. Kieda, C. et al. Stable tumor vessel normalization with pO_2 increase and endothelial PTEN activation by inositol trispyrophosphate brings novel tumor treatment. *J. Molec Med.* **91**, 883–899 (2013).
47. Wang, L. H. V. & Hu, S. Photoacoustic tomography: In vivo imaging from organelles to organs. *Science* **335**, 1458–1462 (2012).
48. Ntziachristos, V. & Razansky, D. Molecular imaging by means of multispectral optoacoustic tomography (MSOT). *Chem. Rev.* **110**, 2783–2794 (2010).
49. Li, M. L. et al. Simultaneous molecular and hypoxia imaging of brain tumors in vivo using spectroscopic photoacoustic tomography. *Proc. IEEE*. **96**, 481–489 (2008).
50. Mirg, S., Turner, K. L., Chen, H. Y., Drew, P. J. & Kothapalli, S. R. Photoacoustic imaging for microcirculation. *Microcirculation* **29**, 6–7 (2022).
51. Rupp, T. et al. Anti-CTLA-4 and anti-PD-1 immunotherapies repress tumor progression in preclinical breast and colon model with independent regulatory T cells response. *Transl Oncol.* **20**, 101405 (2022).
52. Duraiswamy, J., Kaluza, K. M., Freeman, G. J. & Coukos, G. Dual Blockade of PD-1 and CTLA-4 combined with tumor vaccine effectively restores T-cell rejection function in tumors. *Cancer Res.* **73**, 3591–3603 (2013).
53. Doty, D. T. et al. Modeling immune checkpoint inhibitor efficacy in syngeneic mouse tumors in an ex vivo immuno-oncology dynamic environment. *Int. J. Mol. Sci.* **21**, 6478 (2020).
54. Kim, K. et al. Eradication of metastatic mouse cancers resistant to immune checkpoint Blockade by suppression of myeloid-derived cells. *Proc. Natl. Acad. Sci. USA*. **111**, 11774–11779 (2014).
55. Lechner, M. G. et al. Immunogenicity of murine solid tumor models as a defining feature of in vivo behavior and response to immunotherapy. *J. Immunother*. **36**, 477–489 (2013).
56. Chen, Z. et al. TCF-1-centered transcriptional network drives an effector versus exhausted CD8 T cell-fate decision. *Immunity* **51**, 840–55.e5 (2019).
57. Scott, A. C. et al. TOX is a critical regulator of tumour-specific T cell differentiation. *Nature* **571**, 270–274 (2019).
58. Kiraga, Ł. et al. Changes in hypoxia level of CT26 tumors during various stages of development and comparing different methods of hypoxia determination. *PLoS One*. **13**, e0206706 (2018).
59. Gao, J. L. et al. Hypoxia pathway and hypoxia-mediated extensive extramedullary hematopoiesis are involved in ursolic acid's anti-metastatic effect in 4T1 tumor bearing mice. *Oncotarget* **7**, 71802–71816 (2016).
60. Takakusagi, Y. et al. A multimodal molecular Imaigng study evaluates Pharmacological alteration of the tumor microenvironment to improve radiation response. *Cancer Res.* **28**, 6828–6837 (2018).
61. Prasad, O. et al. Multifunctional albumin - MnO2 nanoparticles modulate solid tumor microenvironment by attenuating hypoxia, acidosis, vascular endothelial growth factor and enhance radiation response. *ACS Nano*. **8**, 3202–3212 (2014).
62. Chen, T. et al. Mesoporous radiosensitized nanoprobe for enhanced NIR-II photoacoustic imaging-guided accurate radio-chemotherapy. *Nano Res.* **15**, 4154–4163 (2022).
63. Maslov, K., Zhang, H. F. & Wang, L. V. Effects of wavelength-dependent fluence Attenuation on the noninvasive photoacoustic imaging of hemoglobin oxygen saturation in subcutaneous vasculature in vivo. *Inver Probl.* **23** (6), S113 (2007).
64. Bedinger, A. L., Glowa, C., Peter, J. & Carger, C. P. Photoacoustic imaging to assess pixel-based sO2 distributions in experimental prostate tumors. *J. Biomed. Opt.* **23**, 036009 (2018).
65. Tzoumas, S. et al. Eigenspectra optoacoustic tomography achieves quantitative blood oxygenation imaging deep in tissues. *Nat. Commun.* **7**, 12121 (2016).
66. Jacobetz, M. A. et al. Hyaluronan impairs vascular function and drug delivery in a mouse model of pancreatic cancer. *Gut* **62**, 112–120 (2013).
67. Kieda, C. et al. Stable tumor vessel normalization with pO_2 increase and endothelial PTEN activation by inositol trispyrophosphate brings novel tumor treatment. *J. Mol. Med. (Berl)*. **91**, 883–899 (2013).

68. Hupple, C. W. et al. A light-fluence-independent method for the quantitative analysis of dynamic contrast-enhanced multispectral optoacoustic tomography (DCE MSOT). *Photoacoustics* **10**, 54–64 (2018).
69. Goel, S. et al. Evaluations of radiotherapy in small animal models of pancreatic cancer with oxygen enhanced-dynamic contrast enhanced multispectral optoacoustic tomography (OE-DCE MSOT). *Proc. SPIE.* **12379**, 123791B (2023).
70. Dogan, B. E. & Yang, W. T. Why is breast MRI so controversial? *Curr. Breast Cancer Rep.* **2**, 159–165 (2010).
71. Sung, Y. S. et al. Dynamic contrast-enhanced MRI for oncology drug development. *J. Magn Reson. Imaging.* **44**, 251–264 (2016).
72. Whitaker, K. D., Sheth, D. & Olopade, O. I. Dynamic contrast-enhanced magnetic resonance imaging for risk-stratified screening in women with *BRCA* mutations or high Familial risk for breast cancer: Are we there yet? *Breast Cancer Res. Treat.* **183**, 243–250 (2020).
73. Mann, R. M., Kuhl, C. K. & Moy, L. Contrast-enhanced MRI for breast cancer screening. *J. Magn. Reson. Imaging.* **50**, 377–390 (2019).
74. Monticciolo, D. L., Newell, D. L., Moy, L., Lee, C. S. & Destounis, S. V. Breast cancer screening for women at higher-than-average risk: Updated recommendations from the ACR. *J. Am. Coll. Radiol.* **20**, 902–914 (2023).
75. Neuschler, E. I. et al. A pivotal study of optoacoustic imaging to diagnose benign and malignant breast masses: A new evaluation tool for radiologists. *Radiology* **287**, 398–412 (2018).
76. Fylaktakidou, K. C., Lehn, J. M., Greferath, R. & Nicolau, C. Inositol tripyrophosphate: A new membrane permeant allosteric effector of haemoglobin. *Bioorg. Med. Chem. Lett.* **15**, 1605–1608 (2005).
77. Koumbis, A. E., Duarte, C. D., Nicolau, C. & Lehn, J. M. Tetrakisphosphonates and bisphosphonates of myo-inositol derivatives as allosteric effectors of human hemoglobin: Synthesis, molecular recognition and oxygen release. *ChemMedChem* **6**, 169–180 (2011).

Acknowledgements

The authors thank the MD Anderson Cancer Center Small Animal Imaging Facility and the MD Anderson Cancer Center Advanced Cytometry & Sorting Facility for use of their resources. This work was supported by grants RP190211 and RP220270 from the CPRIT program in the state of Texas, and P30 CA016672 from the NCI/NIH.

Author contributions

R.L.T. and M.D.P. designed the study. R.L.T. developed in vivo tumor models with assistance from F.W.S. X.L. synthesized ITPP. R.L.T. and J.D.L.C. performed in vivo imaging studies. R.L.T. analyzed the imaging results, performed the ex vivo tumor cell analyses, and performed the statistics analysis. R.L.T. and M.D.P. developed the manuscript and all co-authors approved the manuscript.

Declarations

Competing interests

The authors declare no competing interests.

Additional information

Correspondence and requests for materials should be addressed to M.D.P.

Reprints and permissions information is available at www.nature.com/reprints.

Publisher's note Springer Nature remains neutral with regard to jurisdictional claims in published maps and institutional affiliations.